K. Ju

H. L. Hu

R. G. Hirko

E. B. Moore

D. Y. Saiki

R. O. Schwenker

Propagation of 1- μ m Bubbles in Contiguous Disk Devices

Propagation margins of contiguous disk devices fabricated on both single- and double-layer garnet films have been measured. These performance measurements for $1-\mu m$ diameter magnetic bubble propagation were made on devices with cell sizes of 18 and 30 μm^2 . The dependence of bias margin on ion-implantation conditions, material parameters, propagation pattern geometries, and temperature is discussed. Deuterium implantation is introduced, together with a new propagation pattern. Implantation with deuterium induces an anisotropy field change similar to that with hydrogen but with 50% smaller dosage. The new propagation pattern, with sawtooth-shaped tracks, reduces the interaction between charged walls of adjacent propagation tracks, thus resulting in improved performance at low bias fields.

Introduction

Developments in the propagation of magnetic bubbles in contiguous disk (CD) devices have been extensively reported in the literature since the first discovery of the phenomenon in 1972 [1-5]. CD devices utilizing 1- μ m diameter or smaller bubbles appear to constitute a promising technology in the continued search for higher storage densities. In this paper, we present results on the propagation of 1-µm bubbles in CD devices having cell sizes of 18 (4 \times 4.5) and 30 (5 \times 6) μ m². With an 18- μ m² cell size, a 10-mm \times 10-mm chip may contain 4×10^6 bits. Both single- and double-layer films grown by liquid-phase epitaxy (LPE) were used in the experiments. The main emphasis of the paper is on devices with 18-\mu m² cell size fabricated on double-layer materials. However, we also present new insights into the operation of devices with 30- μ m² cell size [2-4], together with preliminary results on devices with $18-\mu m^2$ cell size on a single-layer material. The characterization of ion-implantation damage by means of X-ray and ferromagnetic resonance (FMR) measurements, as well as the unique features of deuterium for implantation, are discussed. Our investigation of

various propagation pattern geometries has led to the development of a pattern with a sawtooth-shaped track which substantially reduces the failure mode in which bubbles jump from one propagation track to another.

Ion-implantation conditions with deuterium and characterization of induced damage

Characteristics of the double-layer and single-layer films used in the experiments are shown in Table 1. In the table, ℓ denotes the characteristic length and Q the quality factor [6], which is the ratio of the uniaxial anisotropy constant to the saturation magnetization of the material. The double-layer approach [3] allows the material parameters of each of the layers to be optimized for the separate functions of storing and driving the magnetic bubbles. Note that the composition of the single-layer film is quite similar to that of the driving layer of the double-layer films except for its higher samarium content. The larger samarium content increases the uniaxial magnetic anisotropy to the extent that it can be used as a storage layer.

Copyright 1981 by International Business Machines Corporation. Copying is permitted without payment of royalty provided that (1) each reproduction is done without alteration and (2) the *Journal* reference and IBM copyright notice are included on the first page. The title and abstract may be used without further permission in computer-based and other information-service systems. Permission to *republish* other excerpts should be obtained from the Editor.

Table 1 Composition and characteristics of garnet films used before and after ion implantation.

	Double-layer films		Single-layer films
	Storage layer	Drive layer	
Composition	$Eu_{0.85}Tm_{1.25}Y_{0.9}Ga_{0.5}$	$Sm_{0.05}Gd_{0.75}Tm_{1.2}Y_{1.0}Ga_{0.4}$	$Sm_{0.2}Gd_{0.6}Tm_{1.3}Y_{0.9}Ga_{0.4}$
Thickness (µm)	0.8	0.36	1.24
Magnetization (kA/m)	49.3	34.5	43.4
ℓ (μm)	0.11	0.15	0.137
Q before implantation	2.6	1.5	2.5
Implantation conditions	64 keV, $9.0 \times 10^{15} D_2^+/cm^2$ 28 keV, $3.4 \times 10^{15} D_2^+/cm^2$ 60 keV, $9.0 \times 10^{13} O^+/cm^2$		110 keV, $1.0 \times 10^{16} \text{ H}_2^+/\text{cm}^2$ 45 keV, $5.0 \times 10^{15} \text{ H}_2^+/\text{cm}^2$ 75 keV, $1.7 \times 10^{15} \text{ He}^+/\text{cm}^2$ 30 keV, $5.3 \times 10^{14} \text{ He}^+/\text{cm}^2$
Change of anisotropy field (kA/m)	-220		-330
Q after implantation	-5.1		-5.0
Comment	annealed at 350°C for 30 minutes after ion implantation		not annealed

Calculations based on LSS (Lindhard, Scharff, and Schiott) theory [7, 8] were performed for multiple ion-implantation conditions which would yield a uniform damage profile throughout the implanted portion of the film. The implant conditions so determined are listed in Table 1. The energy of the deepest implant was fixed by the desired implanted layer thickness, whereas the dosage was determined by matching the peak of the damage to that of the desired damage level, as shown in Fig. 1, Curve A. Here the implantation damage is described by the energy deposited per unit volume through ion-nuclear interactions. The energy and dosage of each of the shallower implants were adjusted to give a combined damage profile which was nearly uniform, as shown in Curve A + B + C of Fig. 1.

The actual implantation profile can be characterized using X-ray and ferromagnetic resonance (FMR) techniques [9]. An X-ray (888) diffraction spectrum was measured for samples implanted according to the conditions just specified. From the spectrum, the fractional change Δa of the lattice constant a induced by the ion implantation was found to be $\Delta a/a = 0.0068$.

The magnetic anisotropy change induced by ion-implantation damage through magnetostriction can be characterized by FMR. The spectrum for the perpendicular

resonance (in which the magnetic field is applied perpendicular to the film plane) of the double-layer film, implanted according to the conditions shown in Fig. 1, is shown in Fig. 2. In Fig. 2, ΔH_k denotes the difference in the anisotropy field before and after ion implantation. In practice, the parallel resonance curve is also used in order to obtain both the gyromagnetic ratio and the magnetic anisotropy field in the film. The implanted Q of -5.1shown in Table 1 was determined this way, under the assumption that the saturation magnetization of the driving layer remains unchanged after implantation. Note that the FMR spectrum has only two pronounced peaks, the larger one being due to the bubble layer of the film and the smaller one to the implanted portion. The lack of other pronounced peaks is attributed to the uniform damage profile produced by the calculated implantation conditions.

Both FMR and X-ray techniques offer convenient ways to characterize ion-implantation effects and, specifically, they yield measurements of the change in anisotropy field and lattice strain. However, the actual damaged depth in the film is best determined by chemical etching [10].

In this study, we have chosen deuterium for the deepest implantation, in contrast to previous work in which either hydrogen or helium was used [1, 5]. In Fig. 3, the

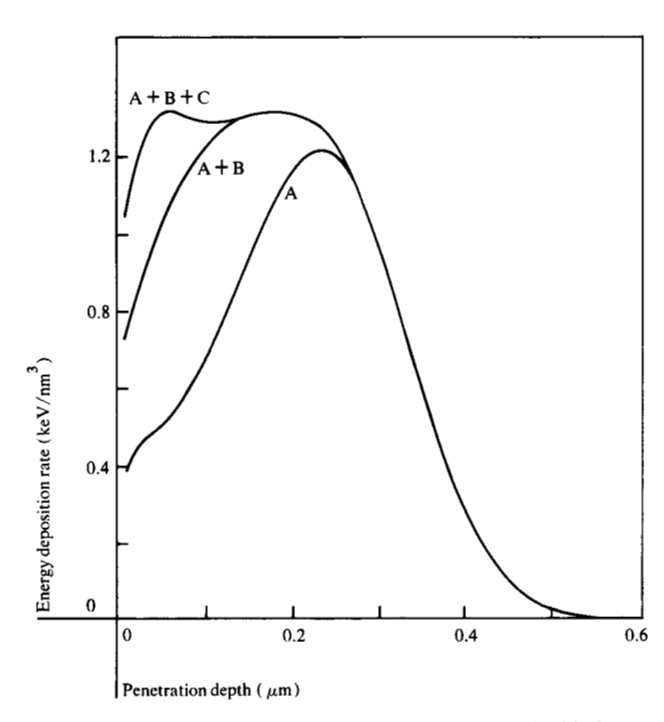


Figure 1 Ion-implantation conditions used for double-layer films. The corresponding calculated damage profiles are shown. Curves A, A + B, and A + B + C correspond to the conditions A alone, A and B together, and A, B, and C together, respectively. Deuterium and oxygen implantation: A: 64 keV, 9×10^{15} D₂⁺/cm², B: 28 keV, 3.4×10^{15} D₂⁺/cm²; C: 60 keV, 9×10^{13} O⁺/cm².

magnetic anisotropy changes (after 350°C annealing) induced by implantation with various ions are plotted against damage level (measured in keV/nm³) in the double-layer film. As the results in Fig. 3 illustrate, the anisotropy field change produced by deuterium, like its isotope hydrogen, and unlike other heavier ions such as helium and boron, shows no saturation with increasing damage level [9]. Since the implantation rate for both species is comparable, and since the implantation time for a 7.6-cm (3-in.) wafer at a beam current of 25 μ A in a typical low-current implantor is measured in hours, the use of deuterium results in a significant improvement in implantation time. Furthermore, only half the hydrogen dose is required if deuterium is used. The two features of nonsaturation and lower dosage are very desirable when scaling down to submicron bubble devices, where a large change of anisotropy field is needed.

Fabrication of ion-implantation propagation structures

The propagation structures were defined with Shipley AZ-1470[®] [11] photoresist implant shielding masks. The resist, about 1.1 μ m thick, was hardened by means of a

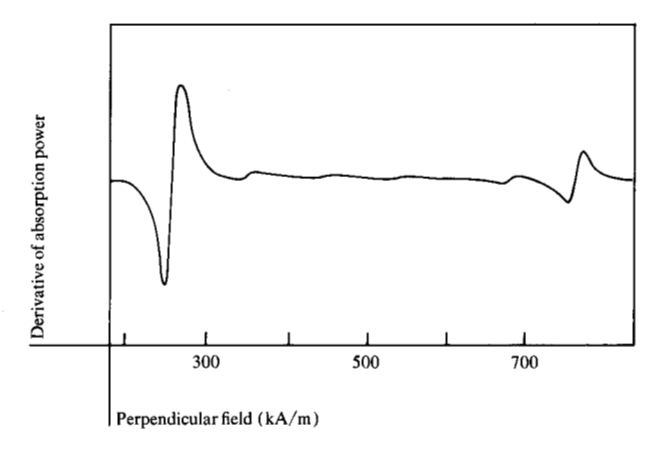


Figure 2 Ferromagnetic resonance (FMR) spectrum for perpendicular resonance of double-layer film after ion implantation. The large resonance on the left corresponds to the storage layer. The resonance to the extreme right corresponds to the implanted drive layer. $\Delta H_k = -229.2 \text{ kA/m}$; Q = -5.1. (Note: 1 kA/m = $4\pi \text{ Oe.}$)

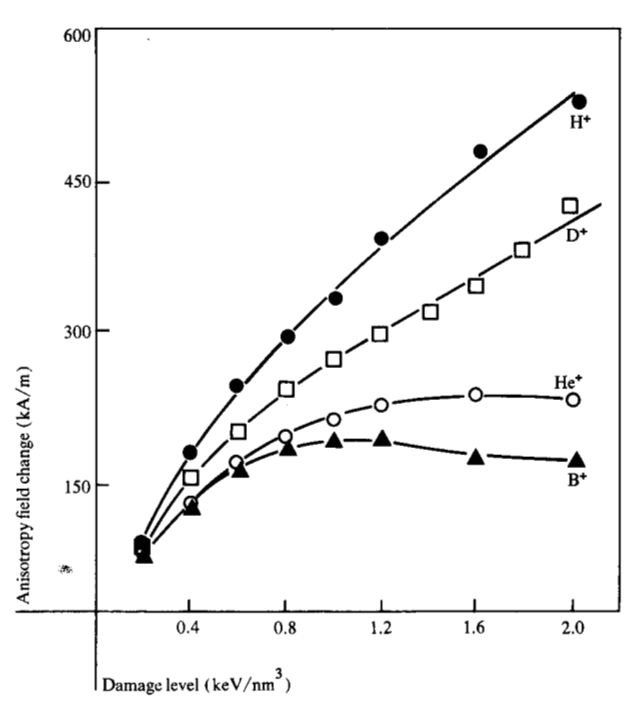


Figure 3 Anisotropy field change $\Delta H_{\rm k}$ vs damage level for various ion species for 350°C annealed samples. Helium, boron, and heavier ions exhibit a saturation in anisotropy field change; hydrogen and deuterium do not.

plasma process prior to ion implantation in order to avoid a shape change of the photoresist patterns during implantation. Other masking materials such as aluminum and gold have also been used, and test results obtained are comparable to those with photoresist masking.

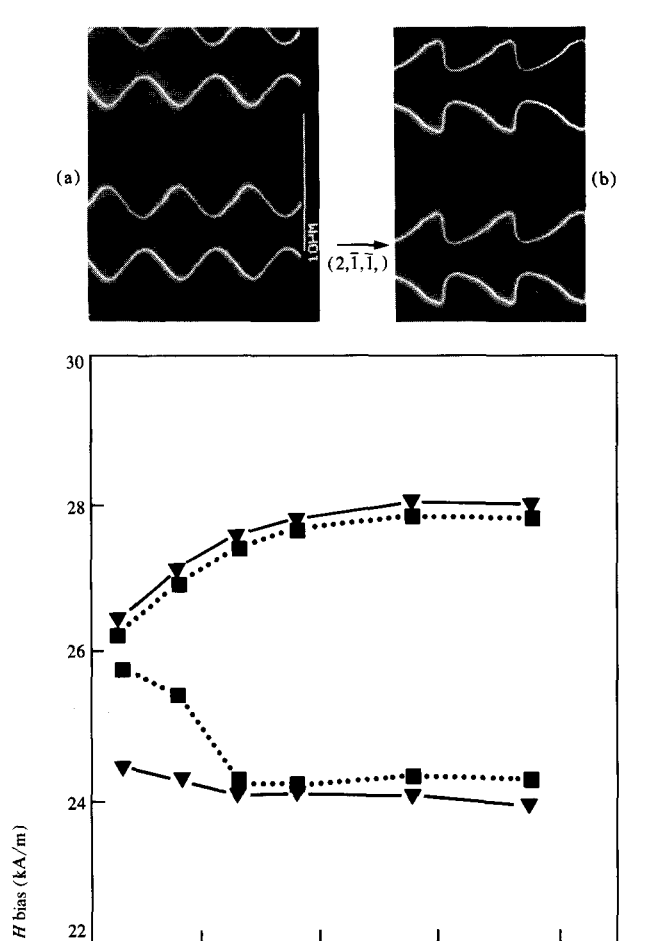


Figure 4 Comparison of bias margins for (1) sinusoidal- and (∇) triangular-shape propagation patterns (30- μ m² cell size). The test conditions are 10⁵ propagation steps at 400 kHz at 25°C. The bias margins are similar to that measured for isolated loops (30- μ m² cell size). Inset: SEM micrograph of propagation patterns with the 30-μm² cell size having (a) sinusoidal and (b) triangular shape.

22

H in-plane (kA/m)

After ion implantation, the photoresist was stripped with plasma ashing, and the sample was annealed at 350°C for 30 minutes. The annealing was necessary in order to stabilize the implantation damage profile against subsequent high-temperature processing steps for a bubble device. An example would be the 350°C deposition of NiFe magnetoresistive thin-film sensors. The samples fabricated on the single-layer film listed in Table 1 were not annealed. Work is under way to study the effects of annealing in single-layer materials.

Dependence of bias margins on propagation patterns, temperature, and ion-implantation conditions

In order to facilitate the comparison of bias margins for several propagation patterns, all test results presented in this section were obtained from the same chip. Similar results have been observed in samples with somewhat different film parameters and ion-implantation conditions. The test conditions, unless otherwise noted, are listed below:

Frequency: 400 kHz

• Propagation steps: 10⁵ with start and stop

 Temperature: 25°C • Drive field: sinusoidal • Data pattern: sparse

The test experiments were performed using visual observation made possible by a low-light-level television camera. Sparse bubble patterns in ten adjacent minor loops, in the case of the 18- μ m² cell size, and eight loops in the case of the 30-µm² cell size, were noted before and after 10⁵ propagation steps at 400 kHz. Each minor loop had a capacity of 125 bits, and had neighboring loops on both sides of the track but no major loops on its ends. The average margin of these loops was used for the data reported here. The sparse data pattern was used for experimental convenience. The margin loss from a sparse data pattern to the worst-case data pattern (that is, fully loaded at the upper end and only single bubble at the low end of the bias field) is approximately 1.5%-2.0% of the mid-bias field for an $18-\mu m^2$ cell size and less than 1% for a 30- μ m² cell size.

• Bias margins for the 30- μm^2 (5 × 6) cell-size devices on double-layer films

SEM micrographs of two 30-\mu m² cell-size propagation patterns are shown in the inset of Fig. 4, the sinusoidal pattern on the left and the triangular pattern on the right. The latter was first introduced by Wolfe et al. [4] and later discussed extensively by Shir [12]. A comparison of the propagation margins for the sinusoidal and triangular patterns is also given in Fig. 4. In general the bias margins for the $30-\mu m^2$ cell size devices reported here are significantly better than those given earlier [3], even though the test criteria are more severe. This improvement in performance may be due to two significant differences in the ion-implantation conditions used. In the present work the use of triple implantations permits a more uniform damage profile. The use of deuterium rather than helium allows a higher change in the anisotropy field. The margins of these two patterns of Fig. 4 are very similar to those of an isolated minor loop. An isolated loop has a larger margin than closely packed loops because the

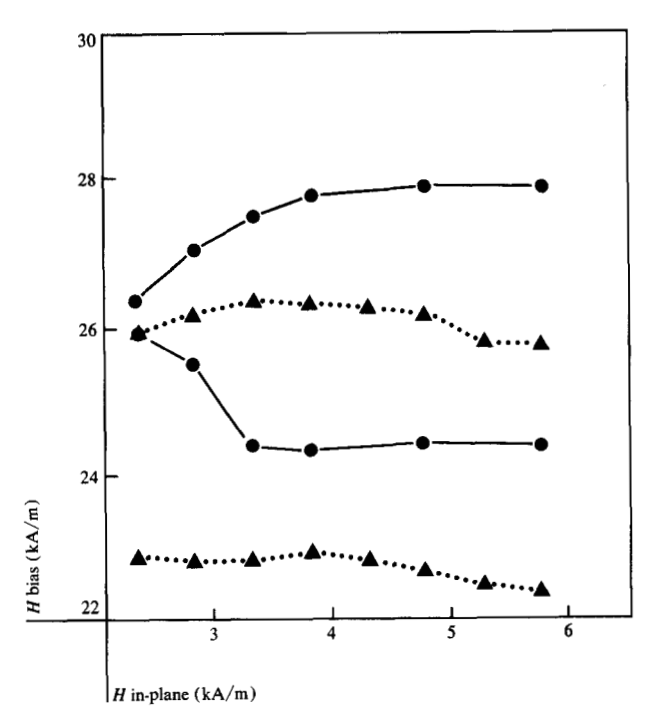


Figure 5 Temperature dependence of bias margins for minor loops of sinusoidal propagation patterns: ●, 25°C; ▲, 70°C.

dominant low-bias field failure mode of bubbles jumping from one track to another cannot occur in the case of the isolated loop. It has been reported [13] that propagation margins at large cell size (such as 64 μ m²) are not very sensitive to the geometry of the propagation pattern. This insensitivity to geometry appears to hold for the 30- μ m² cell size as well. However, this is true only when the ionimplantation damage level is sufficiently high. For example, it was observed that when bias margins for sinusoidal and triangular designs were compared, for patterns fabricated on a similar material but implanted such that the Q was only -3.7, there was a significant loss in bias margin for the sinusoidal pattern. This degradation amounted to about 0.8 kA/m (10 Oe) and occurred at low bias fields. This sensitivity of the performance on pattern geometry suggests that, as the cell size is further decreased, either a higher implantation damage level would be required, or the difference in performance for the two propagation patterns would be accentuated.

The dependence of bias margins on temperature is illustrated in Fig. 5, where it can be seen that the minimum drive field for acceptable performance is lower at higher temperatures. This temperature dependence was also observed in a sample prepared on the single-layer film listed in Table 1. We believe that the nature of

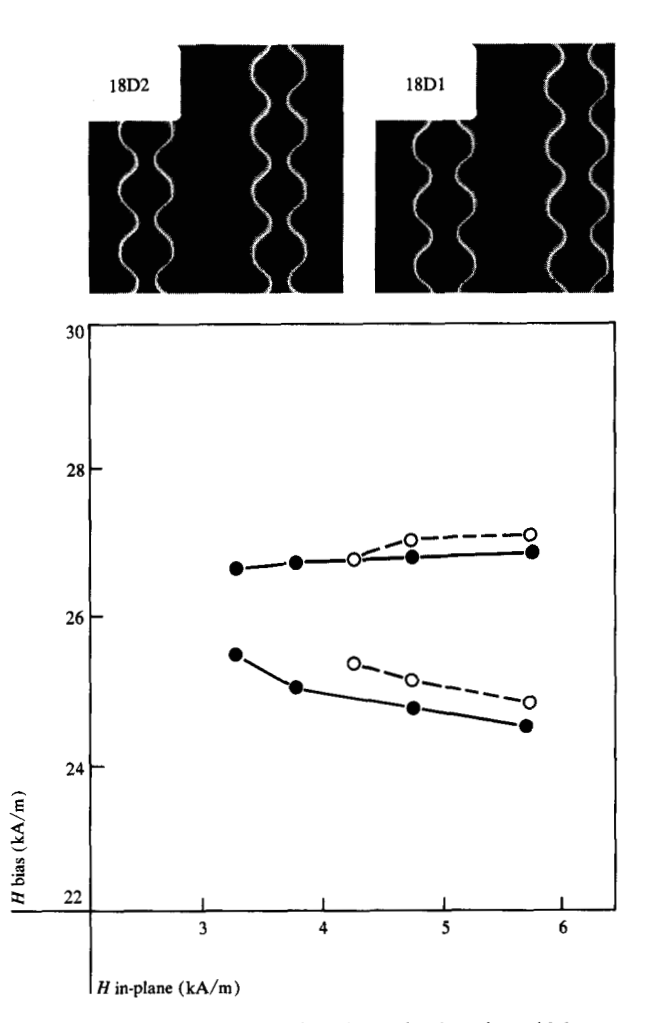


Figure 6 Bias margins for minor loops having sinusoidal patterns shown in the inset: \bullet , 18D1; \bigcirc , 18D2. Inset: SEM micrograph of sinusoidal patterns having 18- μ m² cell size. The cusp offsets of the patterns 18D1 and 18D2 were 1.5 and 1.0 μ m, respectively.

the temperature dependence is due to a decrease of saturation magnetization in the drive layer and/or cubic anisotropy at higher temperatures.

In all, the results presented here for the $30-\mu\text{m}^2$ cell size indicate a good tolerance of device bias margins with respect to operating frequencies, propagation pattern geometries, ion-implantation conditions, and temperature range.

• Bias margins for the 18- μ m² (4 × 4.5) cell size on double-layer films

In Fig. 6, two SEM micrographs of $18-\mu m^2$ cell sizes of sinusoidal geometries are shown together with the propagation margins corresponding to those patterns. The

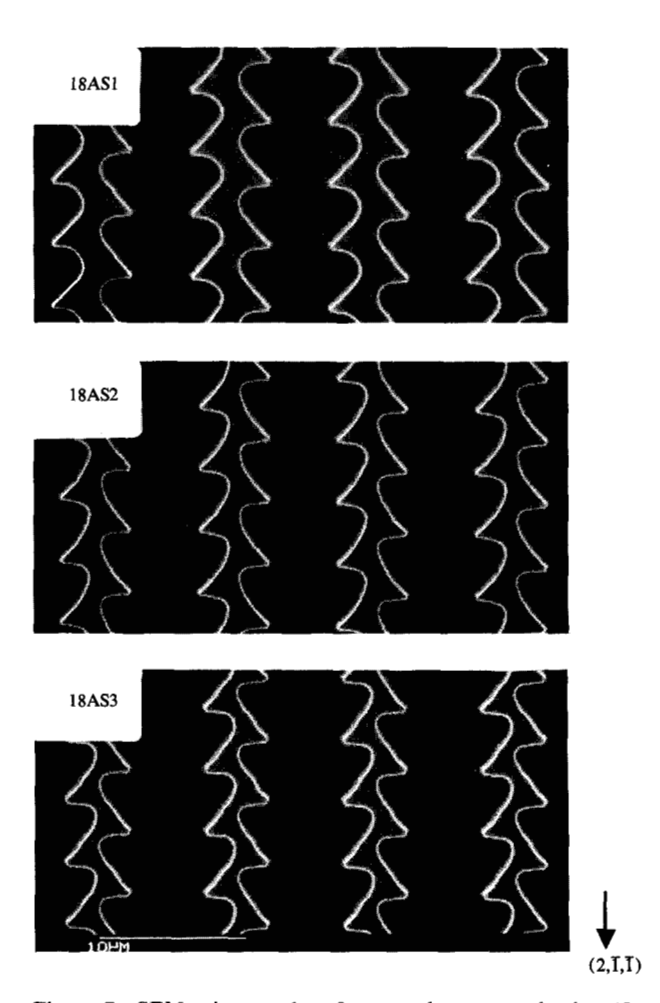


Figure 7 SEM micrographs of sawtooth patterns having 18- μ m² cell size. The cusp offsets for 18AS1, 18AS2, and 18AS3 were 1.0, 0.5, and 0 μ m, respectively.

pattern designated as 18D1 has a cusp offset of 1.5 µm in the photoresist pattern while the other, 18D2, has 1.0 μ m. Here we define the cusp offset to be the distance between two parallel lines drawn tangential to the cusps on each side of a propagation track. The 18D2 pattern is similar to the one reported by Nelson [13]. Note that 18D1 with the larger cusp offset has a higher minimum drive field than the other. In comparing these two designs it is clear that, in pattern 18D2, the area of the nonimplanted region is $0.5 \mu m$ narrower and the implanted area is wider by the same amount. The tendency for those devices with a smaller nonimplanted region and, hence, larger implanted region, to have lower drive requirements has been observed in many device designs. The cause for this phenomenon is thought to be the smaller in-plane demagnetizing field for those patterns with larger implanted regions and/or smaller nonimplanted regions [14, 15]. The margins shown in Fig. 6, however, are considerably smaller than those for the $30-\mu m^2$ cell size shown in Fig. 5.

In an attempt to improve performance, new propagation patterns were designed (see Fig. 7). The implanted region is triangular in shape, similar to that shown in the inset of Fig. 4. The nonimplanted region was made in a "sawtooth" manner in order to maximize the area of the implanted regions for a given track-to-track spacing. Like the SEM micrographs in Fig. 6, the three patterns shown here have successively smaller cusp offsets of 1.0, 0.5, and 0 μ m for 18AS1, 18AS2, and 18AS3, respectively. The implanted region between the tracks is symmetrical in these patterns. Each cusp is oriented in such a way that one of the three crystal axes $(2,\bar{1},\bar{1})$ points into the cusp and bisects the associated angle.

The margins for these three patterns, shown in Fig. 8, are considerably larger than those of Fig. 6. The improvement of margins comes primarily from the low end of the bias field margin, in suppression of the failure mode in which bubbles jump to adjacent tracks. Furthermore, in comparing the three sawtooth patterns, the pattern with the largest implanted region and/or smallest nonimplanted region has the lowest minimum drive field. This is consistent with the results shown in Fig. 6.

The temperature dependence of bias margin for pattern 18AS2 (the one with a cusp offset of $0.5 \mu m$ in the photoresist pattern) is shown in Fig. 9. Again, note the decrease of the minimum drive field when the temperature is increased.

Although the margin for the $18-\mu m^2$ cell size at 70° C is quite good, there is a loss of upper-end bias field margin above 4.8 kA/m (60 Oe) drive field. Such a loss also appears in the 30- μ m² cell size at 70°C (Fig. 5), although at a slightly higher in-plane field of 5.2 kA/m (65 Oe). At 25°C a loss of upper-end bias field margin at high drive fields can also be seen for 18AS3 in Fig. 8. On close examination, it was observed that the failure mode was the same in all three cases and involved bubbles collapsing inside a cusp, or occasionally penetrating into the nonimplanted region and collapsing therein. We conclude that this failure mode is caused by the lack of edge definition between the nonimplanted region and the implanted region at high drive fields. This lack of edge definition can be attributed to too small a nonimplanted region and/or inadequate O in this region. The former reason would explain the behavior of pattern 18AS3 while the latter would apply to the high-temperature region. At elevated temperatures the Q of the nonimplanted region decreases to the point where edge affinity is diminished,

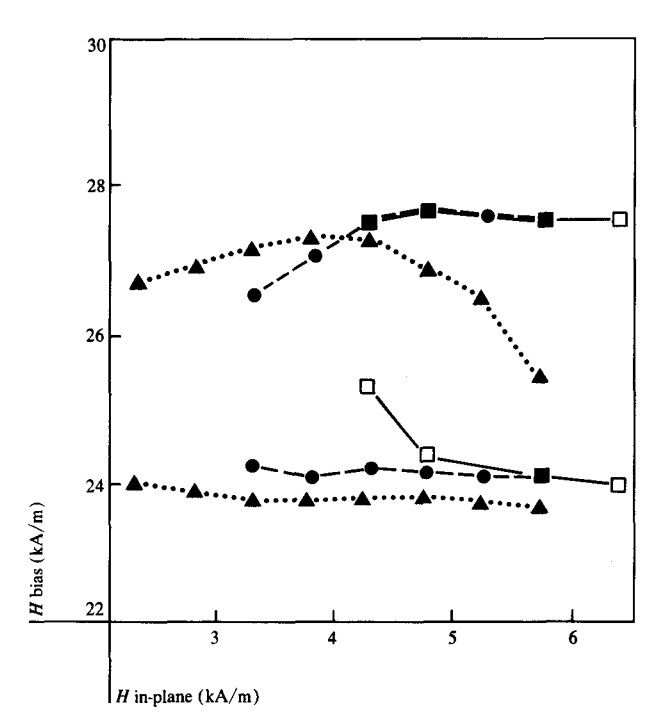
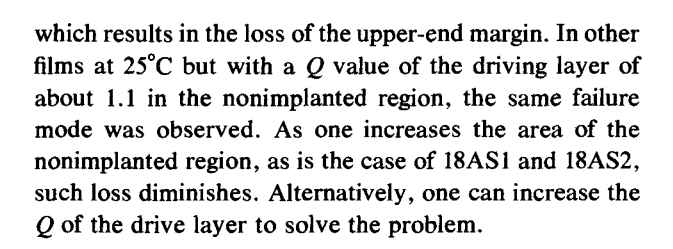


Figure 8 Bias margins for asymmetric minor loops $(18-\mu\text{m}^2\text{ cell size})$ having sawtooth propagation patterns 18AS1 (\square), 18AS2 (\blacksquare), and 18AS3 (\triangle). Shown is the average of 10 inner loops for 10^5 propagation steps at 400 kHz at 25°C. The lower minimum drive field for design 18AS3 is attributed to the larger implanted region for this pattern.



• Single-layer material for the 18- μm^2 (4 \times 4.5) device cell

The bias-field margin for the single-layer material is shown in Fig. 10. Except for a slightly larger minimum drive field, the results are quite comparable to those of the double-layer films shown in Fig. 8. However, the sample used was not annealed, nor were its implantation conditions optimized. The margin for the 18AS3 (Fig. 10) does not show the same performance degradation at high drive fields that was observed on the double-layer material (Fig. 8). This can be attributed to the higher Q in the film.

Summary and conclusions

In summary, both double- and single-layer epitaxial films show good propagation margins for 1- μ m bubbles. For

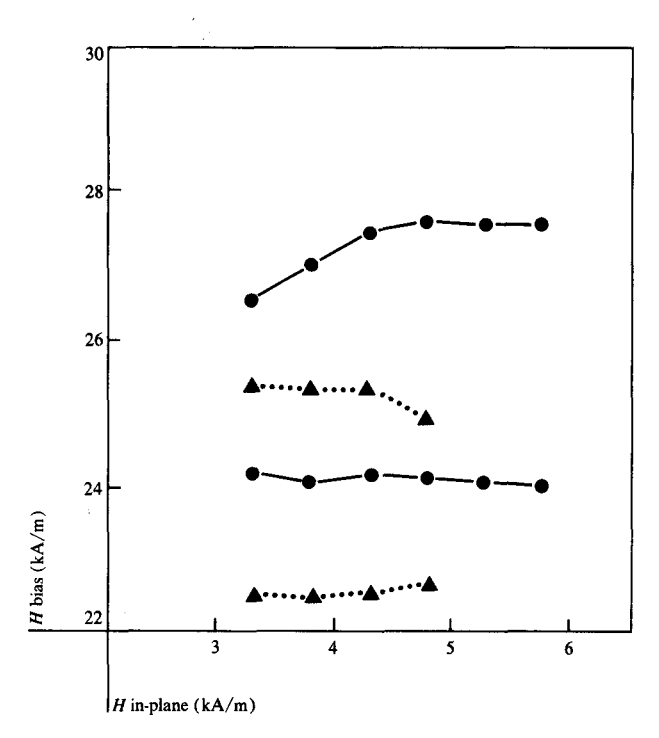


Figure 9 Temperature dependence of bias margins for asymmetric minor loops (18- μ m² cell size) of sawtooth pattern 18AS2: \bullet , 25°C; \blacktriangle , 70°C.

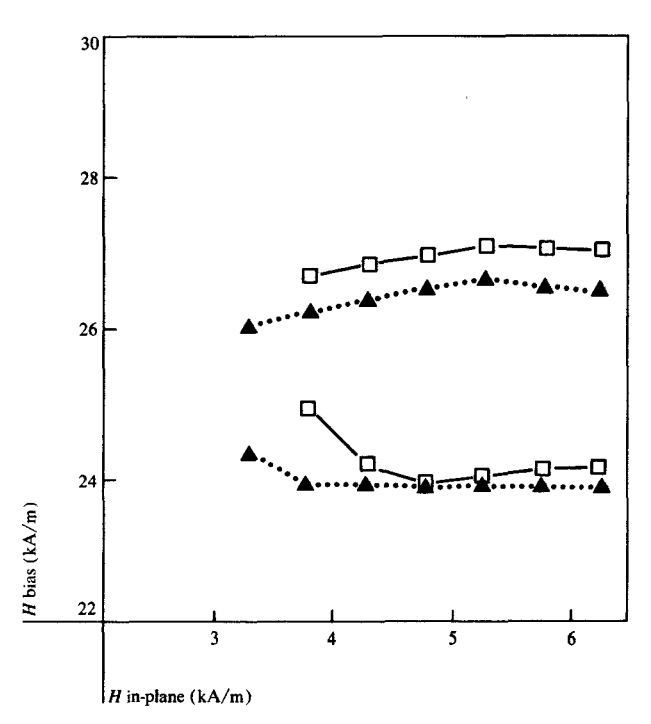


Figure 10 Bias margins for asymmetric sawtooth minor loops (18- μ m² cell size) for propagation patterns 18AS1 (\square) and 18AS3 (\triangle) fabricated on the single epitaxial film.

301

double-layer material, after a 350° C 30-minute anneal, the bias field margins for the $30-\mu m^2$ and $18-\mu m^2$ cell-size devices are 14% and 10% of the mid-bias field, respectively, for the test conditions given below:

• Frequency: 400 kHz

• Propagation steps: 10⁵ with start and stop

• Temperature range: 25-70°C

• Drive field amplitude: 4.0 to 4.8 kA/m (50 to 60 Oe)

• Data pattern: sparse

In addition, deuterium implantation was used because it provided a large anisotropy field change for a considerably smaller dosage compared to hydrogen. The operating margins depend on the geometry and cell size in the following two ways. First, the sawtooth pattern with the triangular implanted region was found to have a superior ion-implantation tolerance, a lower drive field at high frequency, and a better low-end bias margin than that of the sinusoidal pattern. Second, the size of the implanted region between tracks for a given period device strongly affects the minimum drive field for propagation. For an 18-μm² cell-size device, a 1.0-μm increase in the implanted region results in a 0.8-kA/m (10-Oe) reduction in minimum drive field. However, for good bias margin at high drive field and high temperature, a sufficiently high driving layer Q(>1.8) and/or a large enough nonimplanted area are essential.

Acknowledgments

The authors gratefully acknowledge the contributions of P. W. Wang for the X-ray study, C. T. Horng for development of the photoresist process and preparation of the SEM micrographs, W. E. Bogholtz for mask design, and D. E. Horne and W. E. Weresin for designing the electronic test apparatus.

References

- R. Wolfe, J. C. North, W. A. Johnson, R. R. Spiwak, L. J. Varnerin, and R. F. Fischer, "Ion Implanted Patterns for Magnetic Bubble Propagation," Amer. Inst. Phys. Conf. Proc. 10, 339 (1972).
- G. S. Almasi, E. A. Giess, R. J. Hendel, G. E. Keefe, Y. S. Lin, and M. Slusarczuk, "Bubble Domain Propagation Mechanisms in Ion-Implanted Structures," Amer. Inst. Phys. Conf. Proc. 24, 630 (1975).

- Y. S. Lin, G. S. Almasi, and G. E. Keefe, "Manipulation of 1-μm Bubbles with Coarse (>4 μm) Overlay Patterns," J. Appl. Phys. 48, 5201-5208 (1977).
- R. Wolfe and T. J. Nelson, "Crystal Symmetry Effects in Ion-Implanted Propagation Patterns for Magnetic Bubbles," presented at the INTERMAG Conference, Florence, Italy, May 1978.
- Y. S. Lin, G. S. Almasi, G. E. Keefe, and E. W. Pugh, "Self-Aligned Contiguous-Disk Chip Using 1 μm Bubbles and Charged Wall Functions," *IEEE Trans. Magnetics* MAG-15, 1642 (1979).
- A. A. Thiele, "Device Implications of the Theory of Cylindrical Magnetic Domains," Bell Syst. Tech. J. 50, 727-775 (1971)
- J. Lindhard, M. Scharff, and H. E. Schiott, "Range Concepts and Heavy Ion Ranges," Mat. Fys. Medd. Dan. Vid. Selsk. 33, No. 14 (1963).
- 8. K. Ju, R. O. Schwenker, and H. L. Hu, "Damage in Garnet Films Produced by Multiple Ion Implantation," *IEEE Trans. Magnetics* MAG-15, 1658 (1979).
- R. Hirko and K. Ju, "Ion-Implantation Conditions and Annealing Effects for Contiguous Disk Bubble Devices," IEEE Trans. Magnetics MAG-16, 958 (1980).
- W. A. Johnson, J. C. North, and R. Wolfe, "Differential Etching of Ion-Implanted Garnet," J. Appl. Phys. 44, 4753 (1973)
- 11. [®]AZ is a registered trademark of American Hoechst Corp., Route 202-206 No., Somerville, NJ 08876. Their licensed distributor is the Shipley Corp., Newton, MA.
- C. C. Shir, "Triangular Propagation Patterns for Contiguous Disk Magnetic Bubble Devices," presented at the 26th Annual Conference on Magnetism and Magnetic Materials (Paper DB-8), Dallas, TX, 1980.
- T. J. Nelson, D. J. Muehlner, P. I. Bonyhard, J. E. Geusic, V. V. S. Rana, B. J. Roman, G. P. Vella-Coleiro, W. D. P. Wagner, and R. Wolfe, "Ion-Implanted Bubble Chip Functions," presented at the International Conference on Magnetic Bubbles (Paper G-1), Tokyo, Japan, 1980.
- J. S. Best, "Critical Curves for Implanted Garnet Films in the Presence of a Demagnetizing Field," presented at the 26th Annual Conference on Magnetism and Magnetic Materials (Paper DB-9), Dallas, TX, 1980.
- B. A. Calhoun and I. L. Sanders, "Minimum Drive Fields in Contiguous Disk Bubble Devices," presented at the 26th Annual Conference on Magnetism and Magnetic Materials (Paper DB-7), Dallas, TX, 1980.

Received January 16, 1981; revised March 6, 1981

K. Ju, H. L. Hu, R. G. Hirko, D. Y. Saiki, and R. O. Schwenker are located at the IBM Research Division laboratory, San Jose, California 95193. E. B. Moore is located at the IBM General Products Division laboratory, San Jose, California 95193.